Enhanced Detection Performance of a TMR Sensor-Based Metal Detector with the Wavelet Denoising Algorithm

Chenge Ding[1,2], Junqi Gao[1,2], Ying Shen[1,2,*], Zekun Jiang[1,2], Cheng Gao[1,2], Jiamin Chen[3]

[1] Harbin Engineering University, Qingdao Innovation and Development Base, Shandong 266400, China,
[2] Harbin Engineering University, Herbin 150001, China
[3] Chinese Academy of Sciences, Aerospace Information Research Institute, Beijing 100094, China.

Magnetic fingerprint characteristics (MFCs) of active magnetic detection are magnetic signals induced by a metal target that is excited by a primary magnetic field. The detection performance of such a technique is affected mainly by the extraction of MFCs from complex magnetic fields. In this work, we propose a wavelet denoising analysis method to effectively suppress magnetic background noise and extract the MFCs of interest of induced signals in an active magnetic detection system. Moreover, the experimental results demonstrated that the processed wavelet denoising analysis method is consistent with the simulated magnetic dipole model, which can suppress environmental noise to less than 5 nT. The results of the simulations and experiments show that wavelet denoising can effectively remove noise and improve active magnetic detection performance.

***Index Terms*—Active magnetic detection, magnetic fingerprint characteristic, wavelet denoising.**

I. Introduction

ACTIVE magnetic detection technology has been widely used in various fields, including the military[1, 2], security[3], mineral[4, 5], and industry[6, 7] fields. In this technology, extracting magnetic fingerprint characteristics (MFCs) from complex background magnetic fields is the key to successful detection[8]. In detail, the background field mainly consists of the primary excitation field, magnetization field, and environmental noise. Signal denoising is very desirable for suppressing noise components while minimizing the loss of useful signals. Therefore, specific technical approaches are required to suppress electromagnetic interference and geomagnetic noise in signals and improve metal detection performance.

To date, many investigations have focused on analysis methods for signal denoising. Some studies have been performed to design the best configuration of the sensor system to improve detection performance. For example, Yue et al. controlled the distance between the Tunneling Magnetoresistance (TMR) sensor and the center of a circular frame coil to suppress the magnetic induction error caused by position variations[7]. Furthermore, our previous studies demonstrated that TMR sensors exhibit excellent low-noise performance at high frequencies, making them highly suitable for detection systems[9]. On the other hand, some works have developed advanced algorithms to eliminate noise during signal processing, such as matched filtering[10], wavelet transform[11], adaptive interference cancellation techniques[8], and empirical mode decomposition (EMD)[12].

Wavelet denoising is one of the most commonly used methods in denoising analysis. It provides localized analysis in both the time and frequency domains to capture useful signals from noise bands[13]. Shan et al. analyzed the principles of wavelet denoising on the basis of the wavelet transform and magnetic anomaly detection (MAD)[14]. Zhou et al. proposed a method based on orthogonal basis function (OBF) decomposition and wavelet packet denoising for magnetic gradient signals[15]. However, the OBF algorithm is applicable under a Gaussian white noise background. The efficiency of the wavelet denoising method is strongly affected by several parameters, such as the wavelet base function, decomposition levels and thresholding. Moreover, it is critical to establish reasonable parameters to evaluate the results of the denoising process. Gao et al. used multiparameter synergy analysis (MPSA) to select the optimal candidate mother wavelet[16]. Peng et al. elucidated the mathematical relationship between wavelet frequency characteristics and vanishing moments, resulting in an effective notch filter that suppresses high-frequency energy[17]. In the active magnetic detection system, however, the frequency domain components of the measured signals are more complicated and are distributed over a wide span range. Thus, separating useful signals from strong background noise is a major challenge for the wavelet denoising method.

To overcome these limitations, we propose a wavelet denoising analysis method to effectively suppress magnetic background noise in active magnetic detection and analyze the MFC signals of metal targets in the detection area, which enables the detection of small metal target particles from the background field. Moreover, the experimental results demonstrate that the method can accurately detect metal targets in the background of industrial production lines. For the 2-mm metal particles moving at 150 mm/s, the peak SNR of the proposed method reaches 14.73 dB, which is 11.66 dB greater than that of smooth filtering.

The rest of this paper is organized as follows: Section 2 introduces the magnetic fingerprint characteristics and principles of wavelet denoising combined with an RMS. In

This work was supported by National Key R&D Program of China (Grant No. 2021YFB2011600), Natural Science Foundation of Heilongjiang Province (Grant No. YQ2021F001), and National Natural Science Foundation Youth Program (Grant No. 62101151). Corresponding Author: Ying Shen(e-mail: shenying@hrbeu.edu.cn).

Section 3, the experimental setup and results analysis are presented. Finally, this is summarized in Section 4.

II. Theoretical Analysis

A. Model of MFCs

In the near-field region, where the detection intervals are much smaller than the signal wavelength, it is sufficient to approximate the electromagnetic field characteristics once in the detection of small metal objects, as the influence of electromagnetic waves can be neglected [18]. When the detection range exceeds three times the diameter of the metal target, the target can be reasonably modeled as a magnetic dipole, allowing for simplified and effective analysis. Thus, we employ the magnetic dipole model to analyze the frequency characteristics of the magnetic flux density in the induced signals, as illustrated in Fig. 1:

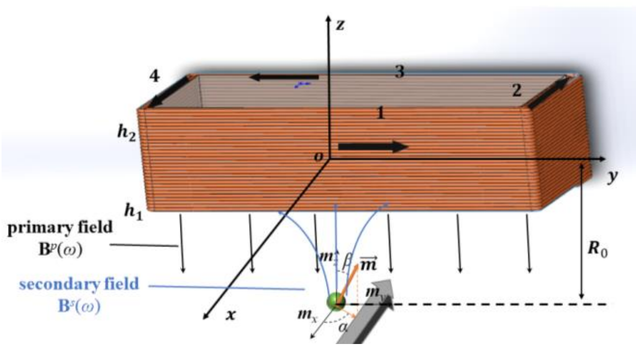

Fig. 1. Model of the excitation magnetic field of a rectangular coil and the induced magnetic field of a metal target.

The excitation coil consists of a multiturn rectangular coil, and the excitation magnetic flux density components $\mathbf{B}_x$, $\mathbf{B}_y$, and $\mathbf{B}_z$ are calculated through volume integration via the Biot-Savart law. The magnetic field information at a certain point in the spatial field can be represented in Cartesian coordinates by integrating the Biot-Savart law over the volume:

$$\mathbf{B}^p = \sum_{i=1}^{4} \frac{\mu_0}{4\pi} \int_{v_i} \frac{\boldsymbol{J}_t\left(x',y',z'\right)\times \boldsymbol{e}_R}{R^2} dv . \quad (1)$$

where $\mu_0 = 4\pi\times10^{-7}$ H/m is the vacuum permeability, and R is the distance vector from the magnetic field information point in space to the coil source point. $\boldsymbol{e}_R$ is the space unit current, and J_t is the current density vector in the coil at t moment and is a time variable with a frequency of ω. By adding the vector sum of the magnetic flux density in the rectangular coil region v_1, v_2, v_3, and v_4, the x, y, and z components of the magnetic field intensity at any point in space can be obtained.

According to previous works, the target can be considered an ideal magnetic dipole when the detection distance is more than 3 times the size of the target [1]. Under excitation by the primary magnetic field, the metal target generates a secondary magnetic field due to both the magnetization effect and the eddy current effect. The characteristics of this secondary magnetic field are influenced primarily by the target's magnetic permeability and electrical conductivity. The magnetic field generated by a magnetic dipole can be described as:

$$\mathbf{B}^s\left(\mathbf{m},\mathbf{r}\right) = \frac{\mu_0}{4\pi}\left[\frac{3\left(\mathbf{m}\cdot\mathbf{r}\right)\mathbf{r}}{R^5} - \frac{\mathbf{m}}{R^3}\right]. \quad (2)$$

where $\mathbf{r}$ represents the distance vector from the target to the measurement point (position of the magnetic sensor) and $\mathbf{m}$ represents the induced magnetic dipole moment of the target. Accordingly, the induced magnetic moment can be expressed as:

$$\mathbf{m} = 2\pi a^3 \chi(\omega)\mathbf{B}^p . \quad (3)$$

where

$$\begin{cases} \chi(\omega) = \dfrac{\left(2\mu_r + 1\right)\left(\sinh\gamma - \gamma\cosh\gamma\right) + \gamma^2\sinh\gamma}{\left(\mu_r - 1\right)\left(\sinh\gamma - \gamma\cosh\gamma\right) - \gamma^2\sinh\gamma} \\ \gamma = \left(i\omega\mu_r\mu_0\delta\right)^{1/2} a \end{cases} . \quad (4)$$

As shown in Fig. 1, α and β represent the directional angle of the induced magnetic dipole moment $\mathbf{m}$, α is used to describe the angle between $\mathbf{m}$ in the *xoy*-plane and the positive direction of the *x-axis*, and β represents the angle between $\mathbf{m}$ and the positive direction of the *z-axis*, where a indicates the diameter of the target. Combining (1), (2), and (3), at t_1, the magnetization field $\mathbf{B}^s$ can be expressed as follows[19]:

$$\begin{aligned} \begin{bmatrix} \mathbf{B}_x^s \\ \mathbf{B}_y^s \\ \mathbf{B}_z^s \end{bmatrix} &= \frac{\mu_0 a^3 \chi(\omega)}{4\pi R^5} \begin{bmatrix} 3x^2 - R^2 & 3xy & 3xz \\ 3xy & 3y^2 - R^2 & 3yz \\ 3xz & 3yz & 3z^2 - R^2 \end{bmatrix} \begin{bmatrix} \mathbf{B}_x^p \\ \mathbf{B}_y^p \\ \mathbf{B}_z^p \end{bmatrix} \\ &= \frac{\mu_0 a^3 \chi(\omega) \boldsymbol{J}_t}{4\pi R^5} \begin{bmatrix} 3x^2 - R^2 & 3xy & 3xz \\ 3xy & 3y^2 - R^2 & 3yz \\ 3xz & 3yz & 3z^2 - R^2 \end{bmatrix} \begin{bmatrix} B_x^p \\ B_y^p \\ B_z^p \end{bmatrix} \end{aligned} . \quad (5)$$

where the symbol μ_r denotes the relative magnetic permeability of the target, ω denotes the frequency of the excitation magnetic field, and a denotes the diameter of the target.

By combining (4) and (5), it can be determined that the amplitude curve of the induced magnetic signal B^s is derived from $\chi(\omega)$, and the frequency of B^s is determined by the current density $\boldsymbol{J}$. On the basis of the model shown in Fig. 1, the target is positioned on the plane of $z = 0$ and moves along the positive direction of the *x-axis* with a velocity of v. By substituting $x = vt$, $y = R_0$, and $z = 0$ into (4), R_0 represents the closest proximity approach (CPA) between the target and the detection point. The total magnetic field B^{sum} of the ω frequency in the measured area is a superposition by the excited magnetic field B^p and the induced magnetic field B^s. Therefore, the expressions for the sum magnetic field signals B_x^{sum}, B_y^{sum}, and B_z^{sum} can be obtained.

$$\begin{bmatrix} B_x^{sum} \\ B_y^{sum} \\ B_z^{sum} \end{bmatrix} = \left\{ \frac{\mu_0 a^3 \chi(\omega)}{4\pi R^5} K + E \right\} \boldsymbol{J}_t \begin{bmatrix} B_x^p \\ B_y^p \\ B_z^p \end{bmatrix} = \left(\xi + E\right) \boldsymbol{J}_t \begin{bmatrix} B_x^p \\ B_y^p \\ B_z^p \end{bmatrix} . \quad (6)$$

where E represents the identity matrix, and K can be described as:

This article has been accepted for publication in IEEE Transactions on Magnetics. This is the author's version which has not been fully edited and content may change prior to final publication. Citation information: DOI 10.1109/TMAG.2024.3520110

$$K=\begin{bmatrix} \frac{2(vt/R_0)^2-1}{\left(1+(vt/R_0)^2\right)^{5/2}} & \frac{3(vt/R_0)}{\left(1+(vt/R_0)^2\right)^{5/2}} & 0 \\ \frac{3(vt/R_0)}{\left(1+(vt/R_0)^2\right)^{5/2}} & \frac{2-(vt/R_0)^2}{\left(1+(vt/R_0)^2\right)^{5/2}} & 0 \\ 0 & 0 & \frac{-(vt/R_0)^2-1}{\left(1+(vt/R_0)^2\right)^{5/2}} \end{bmatrix}. \tag{7}$$

In combination with (6), the expression of B^{sum} can be analogous to the amplitude modulation of B^p; this is verified by the simulation experiment that was conducted to study the induced field of the metal target. In addition, these formulas describe the characteristics of the magnetic field, thereby providing a theoretical foundation for the denoising algorithm. Specifically, these formulas aid in understanding how the magnetic field varies at different frequencies and how to identify and remove noise from the data.

The simulated calculations were conducted to analyze the magnetic field information when a metal iron ball with a diameter of 2 mm passed through a point located 3 cm below the coil, with an excitation frequency of 400 Hz, along the x-axis. The results are shown in Fig. 2.

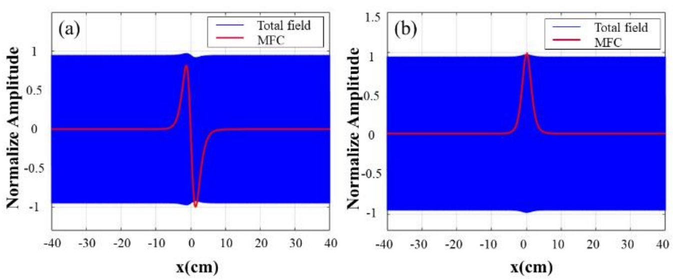

Fig. 2. Target signal of the iron ball: (a) x-axial magnetic field; (b) z-axial magnetic field.

The blue line represents the total magnetic field B^{sum}. The red line represents the induced magnetic field B^s of the metal target, which is defined as the MFCs. Since the target magnetic field B^s_y along the *y-axis* direction remains zero, the normalized magnetic field information is presented for the *x-axis* component B_x^{sum} and the *z-axis* component B_z^{sum}.

B. Wavelet denoising

In practical environments, active magnetic detection signals typically consist of an excitation magnetic field signal, a magnetization field signal, electromagnetic interference, and white noise. The signal $s(n)$ can be expressed as follows:

$$\begin{aligned} s(n) &= A_p\cos(\omega_p n) + A_s\cos(\omega_s n) \\ &+ A_d\cos(\omega_d n) + R_{noise} \end{aligned}. \tag{8}$$

where the symbols ω_p and A_p denote the angular frequency and amplitude of the excitation magnetic field signal, respectively. ω_s and A_s represent the angular frequency and amplitude of the induced magnetic field signal, respectively. Additionally, ω_d and A_d represent the angular frequency and amplitude of the electromagnetic interference component in the environment, respectively, and R_{noise} represents the random noise component, where n is a positive number.

According to Equations (4) and (5), the frequency of the induced magnetic field is derived from the excitation magnetic field. The induced magnetic field signal with a frequency of ω_o is then combined with the excitation magnetic field for analysis. Additionally, on the basis of the simulation results shown in Figure 2 and the Fourier series expansion of the nonperiodic function, the MFC can be interpreted as a formal construction of a multi-order sine harmonic approximation. Therefore, $s(n)$ can be represented as:

$$\begin{aligned} s(n) &= A_s\sum_{i=1}^{k}\xi_i\cos(\omega_{s\_i}n) + (A_p + A_s\xi_{k+1})\cos(\omega_p n) \\ &+ A_d\cos(\omega_d n) + R_{noise} \end{aligned}. \tag{9}$$

where ξ_i, i = 1, 2, …, k and ξ_{k+1} represent the amplitude factors of the harmonic component of the magnetic fingerprint characteristic and the induced magnetic field signal, respectively. ω_{s_i}, where i = 1, 2, …, k are the angular frequencies of the harmonic components of the MFCs.

For sinusoidal signals, when there is a sufficient number of sampling points, the root mean square (RMS) value of the discrete sampled data will be consistent with the effective value of the continuous steady-state signal. In this case, $\cos(\omega_p n)$ will be changed to a constant and merged with R for analysis, and the electromagnetic interference $\cos(\omega_d n)$ will be compressed. On this basis, we set N as an integer multiple of the excitation magnetic field signal period. The RMS analysis signal is represented as follows:

$$\begin{aligned} s_{rms}(n) &= A_{ano}\sum_{i=1}^{k}\xi_{rms\_i}\cos(\omega_{rms\_i}n) + R_{rms\_noise} \\ &+ A_{rms\_d}\cos(\omega_{rms\_d}n) \end{aligned}. \tag{10}$$

where A_{ano}, ξ_{rms_i}, and ω_{rms_i} represent the amplitudes, amplitude factors, and angular frequencies, respectively, of the harmonic components of the MFCs after RMS processing. A_{rms_d} and ω_{rms_d} are the amplitudes and angular frequencies, respectively, of the electromagnetic interference magnetic field component after RMS processing.

In this case, the signal $s_{rms}(n)$ consists of multiple sinusoidal signaling components, representing the MFCs, downshifted electromagnetic environmental noise, and residual noise $R_{\text{rms\_noise}}$ with a baseline. The main characteristic of wavelet transform denoising is its ability to highlight specific features of a problem by transforming the signal and enabling localized analysis. It facilitates the separation of different frequency components that change over time, allowing the extraction of sudden changes occurring at a specific moment. Taking the Haar wavelet function as an example, the signal $s_{rms}(n)$ can be described through the wavelet transform as follows:

$$s_{rms}(n) = \sum_{j=j0}^{n}\sum_{k} d_j(\mathrm{k})\psi_{j,k}(n) + \sum_{k} c_{j0}(\mathrm{k})\varphi_{j0,k}(n). \tag{11}$$

In the wavelet transform, the coefficients d_j and c_{j0} correspond to the approximation and detail coefficients, respectively. The function $\varphi_{j,k}(\mathrm{t}) = 2^{j/2}\varphi(2^j\mathrm{t}-k)$ represents the scaling function, which aims to represent the original signal as accurately as possible via the function $\varphi(x)$. The coefficient $\psi_{j,k}(\mathrm{t}) = 2^{j/2}\psi(2^j\mathrm{t}-k)$ corresponds to the wavelet function, which is used to correct the discrepancies between the scaling function

This article has been accepted for publication in IEEE Transactions on Magnetics. This is the author's version which has not been fully edited and
content may change prior to final publication. Citation information: DOI 10.1109/TMAG.2024.3520110

representation and the original signal

The RMS analysis signal $s_{rms}(n)$ is decomposed into a series of wavelet clusters, and the filtering process is achieved through thresholding and signal reconstruction. By selecting a certain level N of the wavelet $\psi(x)$, the signal undergoes wavelet decomposition. Subsequently, appropriate thresholds are applied to quantize the coefficients d_j at each level, and the reconstructed signal is obtained via the processed coefficients d_j. The simulation results for wavelet denoising of the simulated magnetic field signal are shown in Fig. 3, where wavelet denoising uses the wavelet-based sym4 function for 4-level decomposition.

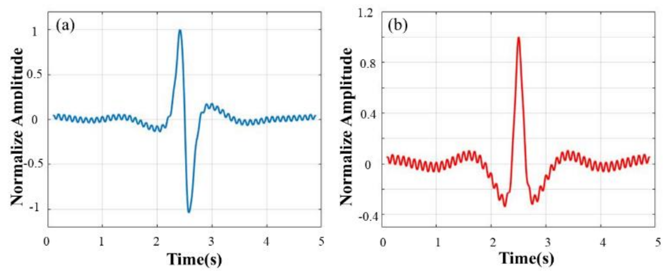

Fig. 3. Wavelet denoising signal of MFCs: (a) x-axial magnetic field; (b) z-axial magnetic field.

On the basis of the aforementioned analysis, the mentioned approach successfully extracts the MFC signal from the magnetic signal at 400 Hz while suppressing the electromagnetic interference and the excitation magnetic field component, and the MFCs remain unaffected. Furthermore, the temporal waveform of signal $s(n)$ is characterized by enhanced relative amplitude and waveform compression.

C. Algorithm

Through the above analysis, the RMS analysis of a sinusoidal signal yields a scalar value, and there is a clear mathematical relationship between the signal strength of a single frequency and the RMS value. As the magnetic field information collected by the magnetic sensor is a multifrequency composite signal, the original signal, when subjected to RMS analysis with a certain N value, exhibits low-frequency signals positioned along a reference line, enhancing the temporal waveform trend of the signal. Wavelet denoising allows for localized analysis in both the time and frequency domains, separating useful signals from noise bands. Therefore, combining RMS analysis with wavelet denoising allows for a significant representation of the MFCs. The processing of the proposed wavelet denoising method is shown in Fig. 4.

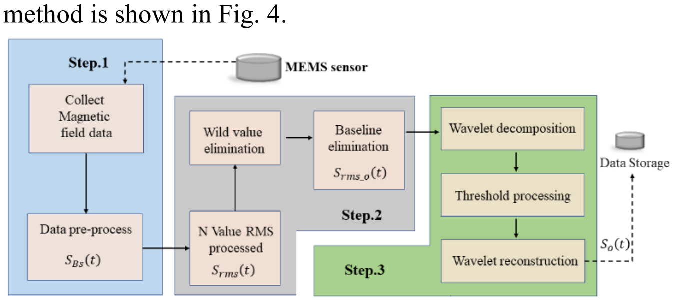

Fig. 4. The signal processing workflow of the proposed wavelet denoising method.

1) *Data preprocessing:*
A Hanning window is applied to the signal to extract the component with the same frequency as that of the excitation magnetic field.

2) *RMS processing of the signal:*
N-point RMS analysis is performed on the preprocessed signal, where N is an integer multiple of the signal period, to eliminate the excitation signal frequency characteristics and extract the signal waveform. Additionally, RMS processing amplifies outlier values at nontarget frequencies (signal frequencies), making them easier to identify and remove.

3) *Wavelet denoising:*
An appropriate wavelet basis function, decomposition scale, and thresholding method are chosen. The decomposition results are evaluated, and the optimized decomposition level is selected. The signal is reconstructed on the basis of the selected decomposition.

III. Experimental Results and Analysis

In practical applications, magnetic signal data are typically collected continuously, and the computational burden of signal processing is directly proportional to the data volume. The MFCs capture the transient response of the metal target under motion. Therefore, the wavelet transform requires a high level of computational capability. To achieve minimal distortion in wavelet denoising and efficient signal selection, it is preferable to use wavelet functions with orthogonal bases, linear phase properties, and symmetry. Orthogonality describes the redundancy of the wavelet function representation, whereas compact support reflects the rich transient characteristics of the signal in the time domain, and the support length is associated with the regularity of the smoothness of the describing function. In this work, we adopt a symmetrical wavelet with an appropriate support range and vanishing moments, as well as good regularity, a linear phase, and compact support properties.

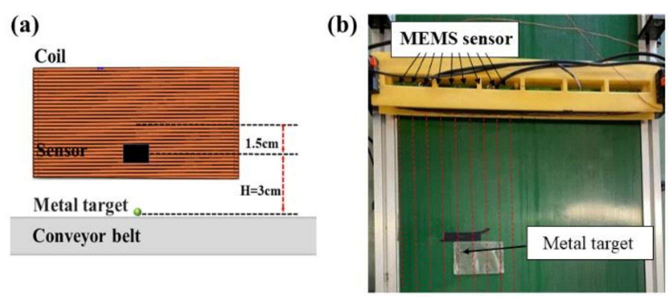

Fig. 5. Schematic diagram of the experiment: (a) y = 0 longitudinal section; (b) experimental platform.

As shown in Fig. 5, the experimental setup mainly consisted of a signal excitation box, a microelectromechanical system array probe that uses a Tunnel Magneto Resistance (TMR9003, MultiDimension Technology Company, Zhangjiagang, China) sensor with a linear range of ± 5 Oe, and a signal acquisition device (USB-6210, National Instruments, USA). The sensor output signal cable is connected to the input port of the USB-6210 and fixed, and then the signal acquisition device is connected to the PC by a USB data cable. The DAQ driver software on the PC side assists in signal acquisition and processing the output of the visual graphical programming software LabVIEW. The signal excitation box (BP4620, NF Corporation, Japan) generates a sinusoidal excitation signal with f = 400 Hz and Vpp = 78 V, which is fed into the excitation coil to generate the excitation magnetic field. It also provides a working voltage of 12 V to the sensor array. The MEMS magnetic sensor array in the rectangular excitation coil is fixed 3 cm above the conveyor belt, with the sensor array placed slightly below the center of the rectangular excitation coil by 1.5 cm. On the basis of the previous analysis, an iron particle with a diameter of 2 mm was used as the metallic target in this study. The output signals of the sensor array are transmitted to the PC end through the acquisition device.

The iron particles continuously passed through the sensor detection area at intervals of approximately 10 s at a speed of

Table 1. The denoising performance data of the symmetrical wavelet

v=150 mm/s, and the resulting data waveforms are shown in Fig. 6. The MFCs can hardly be observed in the time-domain waveform in the original signal, as shown in Fig. 6(a). The signal subjected to RMS analysis exhibits a faint temporal waveform of the MFCs, accompanied by pronounced baseline fluctuations, as shown in Fig. 6(b). Pure wavelet denoising alone has difficulty extracting the signal, mainly because the wavelet transform is suitable for signals with information concentrated in the low-frequency range. When the desired frequency components are in the middle- to high-frequency range, such as for extracting MFCs from the original signal, the spectral window of the wavelet transform in the high-frequency range is wide, containing too many frequency components that are not of interest [13].

Table 1. Denoising data for symmetrical wavelets on the x-components

Level	Wavelet clusters	Refactoring layer	SNR (dB)	Signal Peak(nT)	Noise Peak(nT)
	Sym4		10.82	23.38	6.73
	Sym 5		10.92	23.5	6.69
4-Layer	*Sym* 6	Level 1 Level 2	11	23.59	6.64
	Sym7		11.01	23.65	6.65
	Sym 8		10.92	23.7	6.74
	Sym4		12.63	35.02	8.18
	Sym 5	Level 1	12.43	35.2	8.41
5-Layer	*Sym* 6	Level 2	12.33	35.32	8.55
	Sym7	Level 3	12.25	35.41	8.65
	Sym 8		12.2	35.47	8.71
	Sym4		12.63	35.02	8.18
	Sym 5	Level 2	12.43	35.2	8.41
6-Layer	*Sym* 6	Level 3	12.33	35.32	8.55
	Sym7	Level 4	12.25	35.41	8.65
	Sym 8		12.2	35.47	8.71
	Sym4		12.12	40.47	10.02
	Sym 5	Level 2	11.88	40.48	10.3
7-Layer	*Sym* 6	Level 3	11.72	40.51	10.51
	Sym7	Level 4	11.6	40.56	10.66
	Sym 8	Level 5	11.52	40.59	10.78
	Sym4	Level 2	11.93	40.18	10.15
	Sym 5	Level 3	11.76	40.03	10.34
8-Layer	*Sym* 6	Level 4	11.64	40	10.47
	Sym7	Level 5	11.57	40.04	10.56
	Sym 8	Level 6	11.52	40.07	10.64

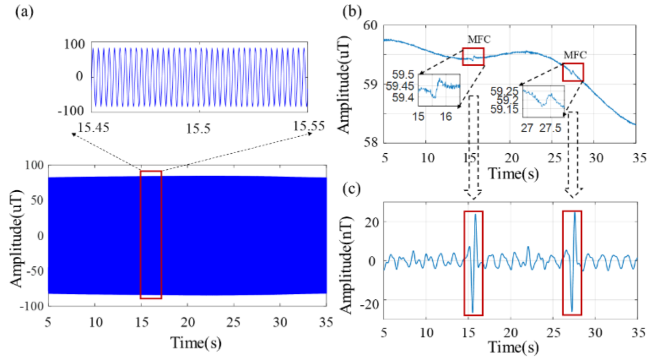

Fig. 6. B_x-component time-domain analysis of the iron particle with a 2 mm diameter: (a) original signal; (b) RMS analysis with N = 60; (c) 6-level denoising using the sym4 wavelet.

Wavelet denoising compresses the frequency range of the MFCs, concentrating the signal spectrum in the low-frequency region. Fig. 6(c) presents the results of wavelet denoising after RMS on the original data, where the MFCs of the iron target exhibit a trend consistent with that of the theoretical analysis and where the environmental noise is suppressed to a level of less than 5 nT. The signal-to-noise ratio (SNR) of the 5-s data analysis and detection before and after the MFC signals are selected, and compared with the SNR of 3.07 dB for the RMS smoothed filtering signal, the peak SNR of the wavelet denoising algorithm proposed in this paper is 12.63 dB. The above wavelet denoising process uses the wavelet-based sym4 function for 4-level decomposition.

To find a symmetrical wavelet basis that is suitable for RMS analysis, sym4 to sym8 wavelet functions with 4 to 8 decomposition levels were analyzed for denoising the x-component of the MFCs while keeping the conditions consistent with RMS analysis, as shown in Fig. 7, and the detailed data are shown in Table 1. Fig. 7 (b) and Fig. 7 (c) show that the peak value of the MFCs increases with increasing decomposition level of the symmetrical wavelet functions for the same case. However, the noise level of the signal also simultaneously increases. Therefore, from the analysis of the SNR in Fig. 7(a), it can be observed that the wavelet function with a decomposition level of 6 achieves a higher peak SNR.

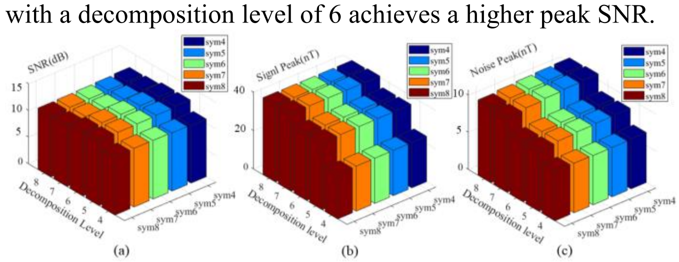

Fig. 7. Denoising performance analysis of the symmetrical wavelet on the x-component: (a) SNR; (b) magnetic signal peak value; (c) noise peak value.

IV. Summary

This paper presents a wavelet denoising method for active magnetic detection. The proposed method is capable of analyzing the magnetic fingerprint characteristics of nongeomagnetic background fields, overcoming the challenge of effectively characterizing the desired signals because of multiple frequency components in wavelet transforms. The feasibility of the proposed method has been validated through experiments and simulations. Additionally, we analyzed the peak SNR, the peak values of the magnetic fingerprint characteristics, and the noise peaks, evaluating the denoising performance of symmetrical wavelet basis functions with 4-8 levels of decomposition. In sym wavelet clusters of the same type, for an excitation frequency of 400 Hz, when the RMS smoothing filter coefficient is 60, the six-layer decomposition of the sym4 wavelet cluster can achieve the best detection SNR. Compared with RMS smooth filtering, the signal-to-noise ratio of the wavelet denoising filter proposed in this paper is improved by 11.83 dB. These analyses provide direct evidence for the feasibility of improving the detection performance of active magnetic sensing.

V. References

[1] L. R. Pasion, “Inversion of Time Domain Electromagnetic Data for the Detection of Unexploded Ordnance,” Ph.D. dissertation, Dept. of Earth, Ocean & Atmospheric Sciences, University of British Columbia, BC, Canada, 2007.

[2] L. Wang, S. Zhang, S. Chen et al., “Underground Target Localization Based on Improved Magnetic Gradient Tensor with Towed Transient Electromagnetic Sensor Array,” IEEE Access, vol. 10, pp. 25025-25033, 2022.

[3] H. B. Hamzah, V. James, S. Manickam et al., “Handheld Metal Detector for Metallic Foreign Body Ingestion in Pediatric Emergency,” Indian Journal of Pediatrics, vol. 85, no. 8, pp. 618-624, Aug, 2018.

[4] B. Kim, S. Jeong, E. Bang et al., “Investigation of Iron Ore Mineral Distribution Using Aero-Magnetic Exploration Techniques: Case Study at Pocheon, Korea,” Minerals, vol. 11, no. 7, Jul, 2021.

[5] A. Zitouni, L. Beheim, R. Huez et al., “Smart Electromagnetic Sensor for Buried Conductive Targets Identification,” IEEE Sensors Journal, vol. 6, no. 6, pp. 1580-1591, 2006.

[6] X. Luo, Z. Liu, H. Zhai et al., “Optimized design of the detection coils for the metal foreign object detection system applied to wireless power transfer,” Energy Reports, vol. 8, pp. 883-890, 2022.

[7] C. Yue, J. Yu, H. Zhang et al., “TMR array with circular skeleton coil for high-current measurement,” Energy Reports, vol. 7, pp. 312-319, Nov, 2021.

[8] D. Liu, X. Xu, C. Huang et al., “Adaptive cancellation of geomagnetic background noise for magnetic anomaly detection using coherence,” Measurement Science and Technology, vol. 26, no. 1, Jan, 2015.

[9] J. Gao, J. Wang, L. Zhang et al., “Magnetic Signature Analysis for Smart Security System Based on TMR Magnetic Sensor Array,” IEEE Sensors Journal, vol. 19, no. 8, pp. 3149-3155, Apr, 2019.

[10] Z. Mao, W. Zhai, Y. Shen et al., “Advanced metal detection system based on TMR sensor array,” Journal of Magnetism and Magnetic Materials, vol. 543, Feb, 2022.

[11] H. Sun, H. Wang, X. Chen et al., "The Application of Curvelet Transform in Noise Suppression of Airbornemagnetic Data," AIP Conference Proceedings, 2017.

[12] B. Dang, C. Liu, L. Yang et al., “EMD-Based Borehole TEM Array Signal Denoising and Baseline Wander Correction for NDT of Downhole Casings,” IEEE Access, vol. 8, pp. 150213-150224, 2020.

[13] T. Guo, T. Zhang, E. Lim et al., “A Review of Wavelet Analysis and Its Applications: Challenges and Opportunities,” IEEE Access, vol. 10, pp. 58869-58903, 2022.

[14] Z. Shan, J. Zhou, J. Chen et al., "Background Noise Suppression of Magnetic Anomaly Signal Based on Wavelet Transform." 2017 IEEE 17th International Conference on Communication Technology (ICCT), pp. 333-337, 2017.

[15] J. Zhou, G. Peng, C. Wang et al., "Magnetic Anomaly Detection Based on Magnetic Gradient Orthonormal Basis Function and Wavelet Packet," 2022 19th International Computer Conference on Wavelet Active Media Technology and Information Processing (ICCWAMTIP), 2022.

[16] J. Gao, L. Sun, S. Zhao et al., “Enhanced ACFM detection performance by multi-parameter synergy analysis,” Insight, vol. 62, no. 2, pp. 81-85, Feb, 2020.

[17] Z. Peng, and G. Wang, “Study on Optimal Selection of Wavelet Vanishing Moments for ECG Denoising,” Scientific Reports, vol. 7, pp. 11, Jul, 2017.

[18] J. R. Wait., “A conducting sphere in a time varying magnetic field,” Geophysics, vol. 16, no. 4, pp. 666-672, Oct, 1951.

[19] J. T. Smith, H. F. Morrison, and A. Becker, “Parametric forms and the inductive response of a permeable conducting sphere,” J. Environ. Eng. Geophys., vol. 9, no. 4, pp. 213-216, Dec, 2004.